

USC-SIPI REPORT #396

Quantification of Self-diffusion Processes in Brain White Tracts with Finite Element Method

by

Shahryar Karimi-Ashtiani

August 2009

**Signal and Image Processing Institute
UNIVERSITY OF SOUTHERN CALIFORNIA
Viterbi School of Engineering
Department of Electrical Engineering-Systems
3740 McClintock Avenue, Suite 400
Los Angeles, CA 90089-2564 U.S.A.**

ABSTRACT

Diffusion MRI (D-MRI) opened a new front for uncovering the convoluted structure of the central nervous system by providing the capability for non-invasive identification of geometries of white tracts in the brain. It is well understood that, this imaging modality is characterized by the shape of the self-diffusion (SD) profile within the brain fibers. Despite previous efforts in the literature for quantification of this physical phenomenon, most current methods suffer from a number of constraints which severely limit the extent of their practical applicability. Here, by relaxing limitations of previous work, we address the solution of the SD process in its most general partial differential equation (PDE) form. To this end, we develop an approach based on the finite elements methodology (FEM) to obtain the numerical SD solution in multi-compartments models of white tracts. Our method provides more flexibility for geometry and material of different white tracts compartments than existing techniques. Due to the finite resolution of D-MRI signals, reconstruction of the SD profile is voxel-wise rather than point-wise. We formulate this problem in terms of parameters of microstructures of white tracts, passing through a voxel. Consequently, the developed method can easily accommodate challenging situations such as tract crossings and demyelinations into computing the voxel aggregate propagators.

Keywords: *Brain imaging, Brain Mapping, Diffusion Tensor imaging, Diffusion magnetic resonance imaging, DTI, Axon.*

INTRODUCTION

During the past two decades, diffusion magnetic resonance imaging (D-MRI) (1-3) has found many applications in diagnoses and studies of abnormalities and diseases associated with the central nervous system (CNS). Example includes, Ischemia (4-6), Multiple Scleroses (7,8), Parkinson's (9), Alzheimer's (10,11) and schizophrenia (12). The D-MRI signal is characterized by the Brownian motion of water molecules within the biological tissues, a process known as self-diffusion (SD). The applicability of this method is rooted in an important assumption that the direction of the SD process is identical to the orientation of the tissues of study. Consequently, the general problem in the study of biological tissues by the D-MRI technology is to assess the tissues structure from the measured SD propagation profile.

The CNS white tract (WT) tissues consist of parallel and well-organized multi-compartment environment which causes the SD process to have directional preference along the WT axonal fibers orientations, which makes them appropriate candidates to be studied by D-MRI. The impacts of the compartments material, geometry packs, and structural parameters, which are in the microscopic scale, are prevalent on aggregate SD propagation profiles in MRI voxels. Inferring the structure of WTs from measured D-MRI signals is often an ill-posed problem. To this end, quantification of the SD process in the WT environment can help identify salient constraints to facilitate the assessment of the WT structure from the incomplete data.

The SD propagation within the WTs has been previously addressed in the literature. The tensor model (13-14) is the most famous experimental approach for the SD characterization within a voxel. Despite its theoretical and practical simplicity, this macroscopic model falls short in accommodating the relation between microscopic WT parameters and the aggregate SD

propagator of a voxel. As an alternative view, there are analytical and numerical measures for the microscopic assessment of the SD process. Due to the complexity of biological tissues, the analytical approaches (15-18) are confined to oversimplified models of WTs which severely limit the extent of their applicability to the practical clinical domain. The Monte Carlo (MC) simulation (19-21) offers a prevalent numerical method to simulate the SD process of water molecules. One of the drawbacks of the MC simulation is its extremely high computational complexity. Hwang et al. (22) addressed the problem by providing a finite difference (FD) solution to the approximate SD partial differential equation (PDE) in the WT environments. However, they provided no quantitative relations between the microscopic SD within the axonal microstructure and the macroscopic aggregate SD regime. Besides, it is well-understood that the FD does not provide an effective technique for the solution of PDEs with irregular boundary conditions such as complex geometries of WTs.

It is fair to say that the solution of PDE of SD propagation under a general geometrical structure of axons has not properly been addressed in the literature. The main difference between solving the SD-based PDE and conducting the MC simulation is that we deal with the average statistical behavior of water molecules in the former approach while we perform the statistical simulation of individual particles in the latter one. It is obvious that the former can dramatically reduce the computational complexity of the latter. Besides, the microscopic parameters (e.g. axons diameters, spacing, myelin thickness, etc.) of WTs are explicitly involved in the SD-based PDE, which makes it possible to easily account for their effects.

To summarize, the intention of our current study is to establish a numerical foundation for the solution of the SD-based PDE with general WT geometries, which imposes no constraints on the axonal models as demanded by previous work. To this end, we devise a PDE solution technique based on the higher-order finite elements methodology (FEM) (23) for the multi-compartment environment of WTs. Our main contributions can be categorized as follows. First, theoretical constraints are devised to make FEM applicable to the solution of the SD-based PDE in multi-compartment environments, which is not automatically held by the standard FEM. Second, we develop a numerical scheme to validate the PDE solution. The relation between the microscopic SD and axonal parameters, and the aggregate SD propagation of an MRI voxel is analytically formulated. The microscopic SD process occurs in the micron range and, unlike its macroscopic aggregate counterpart, is unobservable by D-MRI measurements. Finally, our developed methodology is implemented in form of a software tool, which is applicable to general geometries of axons.

THEORY AND METHOD

It is theoretically well-understood that the observed signal of a D-MRI voxel is strongly tied with the SD profile of spin magnets (e.g., water molecules) within the voxel. Such a relation constitutes the foundation of many applications of this imaging technique for exploring the WT structures in the CNS. For narrow diffusion gradient pulses, the D-MRI principal signal formation is given by the following formula (24),

$$S(k, q) \propto \int_{\mathbb{R}^3} \rho(r') e^{2\pi i k \cdot r'} \int_{\mathbb{R}^3} P_{r'}(r, \Delta) e^{2\pi i q \cdot (r' - r)} dr dr', \quad (1)$$

$$E_{\Delta}(r', q) \propto \mathcal{F}[S(k, q)]. \quad (2)$$

In the above equations, $\rho(r')$ is the concentration of spin magnets, k is the k -space variable, q is proportional to the applied diffusion gradient vector, and Δ is the effective diffusion time during the course of signal acquisition. $S(k, q)$ is the k -space signal which forms a Fourier pair with $E_{\Delta}(r', q)$, the D-MRI signal observed at position r' , as a result of applying diffusion gradient q and effective diffusion time Δ (24-25). The D-MRI signal in Eq. 1 explicitly depends on the SD process through the term $P_{r'}(r, \Delta)$ which is referred to as the SD propagator. It is defined as the probability density function of transition of a water molecule from coordinate position r' at time $t=0$, to position r , at time $t=\Delta$. Throughout this work, notation $P(r, \Delta)$ is used to represent the case where the coordinates origin is shifted to r' ; namely, $r'=0$.

The SD propagator is governed by a second order parabolic PDE (26) as given by

$$\frac{\partial P(r, t)}{\partial t} = \nabla D(r) \nabla P(r, t), \quad (3)$$

where $D(r)$ is the SD coefficient at position r . The solution of the equation can be uniquely specified, if it is accompanied by additional initial and boundary conditions,

$$P(r, t = 0) = \delta(r), \quad (4)$$

$$P(r = \infty, t) = 0. \quad (5)$$

The brain WTs consist of bundles of axons which exhibit different SD speeds at different locations. Consequently, the volume of the tissue of interest is partitioned into a number of compartments such that the SD coefficient is continuous within a compartment, and it has discontinuities on the surface boundaries between neighboring compartments. Hence, the solution of the original PDE in Eq. 3 has to be examined in a multi-compartments scenario. To uniquely identify the solution in such environments, it is necessary to have additional boundary layer constraints for coupling the solutions of two adjacent compartments on their shared boundary (27) as given below

$$J_{\pm}(r) = D_{\pm}(r) \nabla P_{\pm}(r) \cdot \vec{n}(r), \quad (6)$$

where J is the SD probability flow and \vec{n} is the normal vector to the layer surface. The + and – subscripts are used to discriminate quantities on two opposite sides of a layer.

Due to the microstructure complexities of WTs, it is often difficult to find analytical (exact) solutions for the PDE and, therefore, numerical (approximate) techniques have to be exploited inevitably. The higher-order FEMs (23) provide a superior tool for numerical solution of PDEs with boundary conditions defined on complex geometries. Another advantage of this family of methods is that it provides a great degree of flexibility to control the solution precision.

A standard FEM solution consists of three main steps (26): 1) conversion to the variational domain, 2) discretization of the solution and reducing the problem to simple ordinary differential equations (ODEs), and 3) the solution of the ODEs. Since the SD coefficient value in Eq. 3 is discontinuous on layer boundaries between compartments of WTs, the higher order FEM is not directly applicable to our problem in its standard form. However, the FEM includes a host of nice properties which can be employed to devise rules to make a modified FEM applicable to our problem.

As the first step of the FEM solution, the space of the original PDE is transformed to the variational domain by multiplying both sides of Eq. 3 by an arbitrary function $u(r)$ and

integrating over the whole sample volume Ω . For multi-compartment environments, integrating over Ω is equivalent to partitioning the integration domain into the compartment volumes \mathbb{C}_i , as presented in the following,

$$\sum_i \int_{\mathbb{C}_i} \frac{\partial P(r, t)}{\partial t} u(r) dr = \sum_i \int_{\mathbb{C}_i} u(r) \nabla D(r) \nabla P(r, t) dr. \quad (7)$$

Application of the divergence theorem (26) reduces the order of spatial derivatives as shown below,

$$\sum_i \int_{\mathbb{C}_i} \frac{\partial P(r, t)}{\partial t} u(r) dr = \sum_i \left[- \int_{\mathbb{C}_i} D(r) \nabla u(r) \cdot \nabla P(r, t) dr + \int_{S_i} u(r) D(r) \nabla P(r, t) \cdot \vec{dS} \right], \quad (8)$$

where S_i is the surface of \mathbb{C}_i . For the exact solution, the application of layer boundary conditions in Eq. 6 eliminates the surface integral on the right hand side of Eq. 8. However, for approximate (FEM) solutions, this property does not automatically hold, and the design of the solution must be adapted to contain the property. To understand how this constraint is imposed on the approximate solution, it is important to understand the properties of the FEM and design the approximate solution such that it accounts for the layer boundary conditions.

In the FEM, the spatial domain is partitioned into non-overlapping small 3D volumetric shapes which are referred to as elements. Fig. 1 shows a tetrahedral element employed for the experiments of this study. Within an element, the solution is approximated by a linear combination of a finite number of polynomial basis functions, and the global solution is approximated by a linear combination of all basis functions of all elements as given by

$$P(r, t) = \sum_{i=1}^N \alpha_i(t) \varphi_i(r), \quad (9)$$

where α_i values are coefficients to be determined by the solution, and φ_i s are the polynomial basis functions. For the tetrahedral element, different polynomial bases can be defined for the element vertices (lower order bases), as well as for the element edges, faces, and interior regions (higher-order bases). For more details, we refer to (23).

For accommodation of the layer boundary conditions by the FEM approximate solution in Eq. 9, we devise two theoretical rules which are elaborated in Appendix B. It is shown that upon fulfillment of those rules, the surface integrals in Eq. 8 is eliminated and the original PDE in Eq. 3 reduces to a simple linear time invariant (LTI) ODE (26), as summarized by

$$\begin{aligned} S \underline{\alpha}' &= M \underline{\alpha}, \\ \underline{\alpha} &= [\alpha_1(t), \dots, \alpha_N(t)], \end{aligned} \quad (10)$$

where $\underline{\alpha}$ is a vector of coefficients of the basis functions in Eq. 9. The stiffness and mass matrices, denoted by S and M , are large squared sparse matrices of constant entries for two sides of Eq. 22.

The value of $\underline{\alpha}$ at time $t=0$ is exploited to initialize the ODE system. This vector can be calculated by projecting the initial condition function in Eq. 4 into the space of basis functions of the FEM. This is accomplished by minimization of a norm distance between the actual initial function and approximate representation as presented by

$$\left\| P(r, t = 0) - \sum_i \alpha_i(t = 0) \varphi_i(r) \right\|_H, \quad (11)$$

where $\|\cdot\|_H$ is the appropriate norm defined on function space H . The choice of the function space is according to the nature of the problem (e.g. the Sobolev space)(26).

Considering that the initial value function is in form of the Dirac delta function, its approximation by a linear combination of piecewise polynomials is inaccurate. On the other hand, the SD propagator is essentially a probability density function whose integration over the global spatial domain must be one at all time instances. This conservation rule for the propagator is implied by the original PDE in Eq. 3, and no extra explicit mechanism is available to enforce this property. As a result, any error induced in the calculation of the initial value vector, will be preserved and propagated as time evolves. To this end, it is crucial to suppress the error of the initial value function approximation. To address this issue, we narrow our attention on small time interval $[0, t_\varepsilon]$, where t_ε is a small time right after initial time $t=0$. If t_ε is sufficiently small such that water molecules do not find enough time to arrive at any restricting layer boundaries, the SD will be free (unrestricted) (24) during the time interval (see Appendix C for a formal proof). Then, the analytical closed-form solution of free SD (24) can be exploited for evaluation of the propagator values as given below,

$$P_{free}(r, t) = (4\pi Dt)^{-3/2} e^{-r^2/(4Dt)}, \quad t \in [0, t_\varepsilon]. \quad (12)$$

As a result, if the system is initialized at time $t=t_\varepsilon$ with initial value function $P_{free}(r, t_\varepsilon)$, the solution must be unchanged (namely, the ODE is LTI). The advantage of this time shift is that the initial value function is now of the exponential form, whose approximation by a linear combination of piecewise polynomials is far more accurate than the original Delta function. For assessment of reasonable values for t_ε the Einstein equation (24) can be utilized.

$$l = \sqrt{2Dt_\varepsilon}, \quad (13)$$

where l is the distance of the point of interest within the compartment to the nearest layer boundary.

Validation

For general geometry of WTs, validation of the FEM solution is a challenging task due to the lack of ground truth. A valid solution is identified if it satisfies Eqs. 3-5 (28). The initial value condition is realized by delayed-initialization as introduced previously. Since the FEM mesh generation is performed in the finite spatial domain, it implies that the value of the solution is equal to zero at infinity. Hence, the boundary condition of Eq. 5 is satisfied, too. Therefore, the necessary and sufficient condition for a valid solution is that it conforms with the original PDE of Eq. 3. It can be shown that for a compartment with constant SD coefficient D_{C_i} , the original PDE reduces to the following simple relation,

$$D_{C_i} = \frac{\partial P(r, t)/\partial t}{\nabla^2 P(r, t)}. \quad (14)$$

The FEM provides the temporal and spatial evolutions of the solution, which makes it possible to numerically calculate the partial derivatives in Eq. 14. For multi-compartment diffusive environments, a valid solution must confirm in Eq. 3 (or Eq. 14 for the case of constant SD coefficient) in all compartments.

Voxel Aggregate SD Propagator

From Eqs.1 and 2, the ideal (infinite resolution) DMRI signal formation at position r' is given by

$$E(r', \Delta, q) \propto \rho(r') \int_{\mathbb{R}^3} P_{r'}(r, \Delta) e^{2\pi i q \cdot (r-r')} dr. \quad (15)$$

However, due to practical limitations (25), the K -space sampling is often imperfect and the reconstruction of the signal is prone to local averaging over a voxel. Hence, an estimate of the observed D-MRI signal in voxel V_j could be obtained by averaging Eq. 15 over all spin magnets of the voxel,

$$\begin{aligned} E_{V_j}^{av}(\Delta, q) &\propto \frac{1}{N_j} \int_{V_j} \int_{\mathbb{R}^3} \rho(r') P_{r'}(r, \Delta) e^{2\pi i q \cdot (r-r')} dr dr' \\ &= \int_{\mathbb{R}^3} e^{2\pi i q \cdot R} \underbrace{\left\{ \frac{1}{N_j} \int_{V_j} \rho(r') P_{r'}(r' + R, \Delta) dr' \right\}}_{\bar{P}_{V_j}(R, \Delta)} dR, \end{aligned} \quad (16)$$

where $N_j = \int_{V_j} \rho(r') dr'$, denotes the total number of spin magnets in the voxel, and $\bar{P}_{V_j}(R, \Delta)$ is the weighted average of the propagator over voxel V_j . It is known (15) that for long term SD processes, the concentration parameter $\rho(r')$ is uniform over the entire region of a compartment. Therefore, it is possible to evaluate the average voxel propagator by partitioning the voxel volume into its constituting compartments,

$$\begin{aligned} \bar{P}_{V_j}(R, \Delta) &= \frac{1}{N_j} \sum_k \rho_k \int_{C_k} P_{r'}(r' + R, \Delta) dr' \\ &= \sum_k f_k \bar{P}_k(R, \Delta), \end{aligned} \quad (17)$$

where ρ_k is the constant concentration parameter, $f_k = \frac{\rho_k V_k}{\sum_m \rho_m V_m}$ is the spin magnet fraction (V_k is the volume of compartment k confined to the voxel region), and $\bar{P}_k(R, \Delta)$ is the average propagator of compartment k .

RESULTS AND DISSCUSION

The hexagonal-array-of-cylinders (15,22) model is utilized for modeling the WT's environment in our computer simulation study, although far more complex axonal geometries can be handled with the developed method. In this model, a myelinated axon is represented by an inner cylinder as the cell cytoplasm region, and a coaxial cylindrical sheath that models the thick myelin layer around the axon cell. The effect of the axon membrane's partial permeability is lumped into the

permeability of the myelin sheath. The organization of myelinated axons within a WT is assumed to be hexagonal as illustrated in Fig. 2. It is further assumed that the SD coefficient is constant within a compartment (three different compartments identified in the provided model which are cytoplasm, myelin sheath, and extracellular regions). A sample discretization of this model by tetrahedral elements (tetrahedralization) is illustrated in Fig. 1.

For experiments of this study, unless otherwise specified, the following parameters settings will be employed. The sample dimensions (i.e., the volume over which the PDE solution is evaluated) are set to $15 \times 15 \times 15 \mu\text{m}$ along the x-, y-, and z-axes, respectively. The radii of inner cylinders corresponding to cytoplasm regions are set to $R_{in} = 3 \mu\text{m}$, and the radii of myelinated axons are set to $R_{out} = 4 \mu\text{m}$. For the hexagonal organization of axons within a white tract, the distance between the axels of two neighboring cylinders is chosen to be $L = 10 \mu\text{m}$. The SD coefficients for the cytoplasm, myelin, and extracellular regions are selected as $D_c = 1.0 \mu\text{m}^2/\text{ms}$, $D_m = 0.05 \mu\text{m}^2/\text{ms}$, and $D_e = 1.9 \mu\text{m}^2/\text{ms}$, respectively. Following the parameterization for water concentrations in (15), the concentrations of water molecules are set to $\rho_c = 0.85$, $\rho_m = 0.5$, $\rho_e = 0.9$, and $\rho_g = 0.9$ for the cytoplasm, myelin, extracellular, and off-tract regions, respectively. Tetrahedral elements are utilized for construction of the sample mesh of the FEM. In order to relax the minimum rule of conformity to the Sobolev space (see Appendix A), the maximum degree of polynomial functions for the edge, face, and bubble bases are set to $p_e = 3$, $p_f = 4$ and $p_b = 0$, respectively. For the solution of the ODE system in Eq. 10, the high-order implicit Rung-Kutta method was employed.

Fig. 3 specifies the transverse SD propagator – the probability of propagation in the plane perpendicular to the axons orientation - at the center of an axon (position 1 in Fig. 2) after time elapses by $t = 15 \text{ ms}$. The effect of the myelin sheaths around the axon cells in characterization of the profile is evident and they, as a result of their partial permeability, form the shapes of the propagators in the neighboring cytoplasm and extracellular regions.

In Fig. 4 the behavior of the SD propagator as a function of spatial and temporal variables is represented. Since the propagation along the axons orientation encounters no limitation, the evolution of the parallel SD profile always stays close to the Gaussian shapes. On the other hand, as a result of the partial permeability of myelin sheaths, there are drastic deviations from Gaussianity in the transverse propagators. Discontinuities of the transverse propagator at boundaries between compartments are indications of accommodation of layer boundary conditions by our devised methods (see Appendix B).

It was stated before that a valid solution is identified if and only if it confirms in the original PDE in Eq. 3 in all compartments and all positions. For the hexagonal-array-of-cylinders model, the original PDE reduces to a simple relation given by Eq. 14. The practical approach is to perform the evaluations at several sample points of a compartment and study the results statistics (e.g. means and standard deviations). In Fig. 5, evaluation results for the SD propagator at the center of an axon (position 1 in Fig. 2) performed at cytoplasm and myelin compartments are presented. We see that the results of the cytoplasm region are in the valid range from the beginning, whereas it takes about 5 ms to have accurate outcomes in the myelin region. This delay is caused by the time which takes water molecules to depart from the center of the axon and arrive at the myelin region.

In Fig. 6, the aggregate SD propagators in different compartments of a voxel, as results of Eq. 17, are presented. For computation of a compartment aggregate propagator, discrete integration techniques are employed. To evaluate the propagators in the regions of a voxel that are not parts of the passing tract(s), an isotropic propagator model, as provided in Eq. 12, is considered. It can

be seen from the 1D and 3D voxel aggregate propagator profile that the SD process is quite anisotropic along the axons orientation. Also, the role of the myelin region in overall voxel SD anisotropy is downplayed by the small degree of anisotropy of those regions, as well as their low level of water molecules concentrations (see Eq. 17). Also, the extracellular regions exhibit large transverse propagation, which is due to spacing among axons. In Fig. 7 the voxel aggregate propagator for the case of crossing tracts is presented. In Fig. 8, it is shown that how our method can be utilized for studies of nerves degeneration, such as axons demyelinations. It is illustrated that, as a result of the damage to the myelin layer around the axon, the resultant SD propagator becomes severely lateral. This raises serious questions about accuracy of symmetric models, such as the tensor model, for studies of these asymmetric conditions.

CONCLUSION AND FUTURE WORK

In this work, we developed a method based of the FEM technology for the solution of SD-based PDE in the brain WT's environment. We relaxed a lot of constraints imposed by the previous solutions on axonal microstructure geometries and material and extended a method to accommodate more realistic models of WT's. One of the highlights of this work is the formulization of the relations between the WT's microstructure parameters and voxels aggregate SD profile. This relationship is especially important since one can potentially assess unobservable axonal microgeometries from aggregate values of SD propagators over a voxel which are observable by D-MRI measurements. In the developed method, the capacity of including a large degree of variability in WT's structures makes it possible to study the effects of a number of WT's parameters on the SD propagator.

As direct extensions of this work, we intend to include more axonal parameters such as effects of membrane partial permeability as well as non-scalar SD coefficients for the myelin sheaths regions. Also, we will extend the devised methodology to more general D-MRI data acquisition parameter setting such as wide gradient pulses.

APPENDIX A: MINIMUM RULE OF CONFORMITY TO THE SOBOLEV SPACE

The minimum rule is a constraint placed on the FEM basis functions to guarantee the smoothness of the solution. A common criterion for smoothness is the existence and square-integrability of spatial partial derivatives of the solution. This is also known as H^1 conformity or conformity to the Sobolev space. In the case of tetrahedral elements, it can be shown (23) that the sufficient condition for conformity to the Sobolev space is fulfillment of the following inequalities for all tetrahedrons,

$$p^{ej} \leq p^{si} \leq p^b, \quad (18)$$

where p^{ej} , p^{si} , and p^b are the maximum degrees of polynomials associated with the tetrahedron edges, faces, and interior regions, respectively.

APPENDIX B: VARIATIONAL FORMULATION

In this section, our devised rules for accommodation of layer boundary conditions by the FEM approximate solution in Eq. 9 are presented. Let us consider a 2D element which is intersected by a layer boundary as illustrated in Fig. 9 (the result of this section can readily be extended to 3D problems). For a position inside the 2D element, the FEM solution is smooth (polynomial

function), and applying the layer boundary condition in Eq. 6 results the following contradiction on the layer boundary,

$$\begin{cases} D_+ \nabla P_+ \cdot \vec{n} = D_- \nabla P_- \cdot \vec{n} \\ \nabla P_+ = \nabla P_- \end{cases} \implies D_+ = D_- \quad \text{Contradiction! ,} \quad (19)$$

since the value of SD coefficient on the layer boundary has discontinuity by the assumptions. Therefore, as our first devised rule, in the generation of the FEM meshes, no element is divided by the layer boundaries as illustrated in Fig. 9.

As specified in Appendix A, the minimum rule guarantees the smoothness of the FEM solution everywhere, including on elements boundaries. This smoothness can fail our first devised rule on the layer boundaries. To this end, as the second devised rule, the minimum rule must be violated in the design of elements polynomial bases.

Accounting for the first and second devised rules, the layer boundary conditions are included and the surface integrals in Eq. 8 are eliminated which simplified the variational formulations as given by,

$$\int_{\Omega} P_t u \, dr = - \int_{\Omega} D(r) \nabla u \cdot \nabla P \, dr, \quad (20)$$

$$\sum_j \int_{K_j} P_t u \, dr = - \sum_j \int_{K_j} D_j \nabla u \cdot \nabla P \, dr, \quad (21)$$

where K_j is the spatial region confined to the element j . Substituting the approximate FEM solution into Eq. 21 results the following,

$$\begin{aligned} \sum_{n=1}^N \alpha_n(t) \sum_j |J_{K_j}| \int_{\bar{K}} \tilde{\theta}_q^j \tilde{\theta}_n^j \, d\xi &= - \sum_{n=1}^N \alpha_n(t) \sum_j |J_{K_j}| D_j \cdot \\ &\sum_{m=1}^3 \sum_{s=1}^3 \sum_{m=1}^3 \frac{\partial \xi_s}{\partial x_m} \frac{\partial \xi_r}{\partial x_m} \int_{\bar{K}} \frac{\partial \tilde{\theta}_n^j}{\partial \xi_s} \frac{\partial \tilde{\theta}_q^j}{\partial \xi_r} \, d\xi \end{aligned} \quad (22)$$

For $q=1, \dots, N$,

where $|J_{K_i}|$ is the Jacobean, and $\frac{\partial \xi_m}{\partial x_n}$ is the entries of the inverse of the Jacobi matrix of the isoparametric map associated with element K_i (23), and $\tilde{\theta}_n^j = \varphi_n \circ x^{-1}_{K_j}$, and where x_{K_j} is the isoparametric map from the reference element to element K_i , and φ_n 's are the basis functions of the reference element (23,26). Note that Eq. 22 can be reformulated in a simple ODE form (23).

APPENDIX C. INITIAL UNRESTRICTED SELF-DIFFUSION REGIME

We consider a three-compartment environment with SD coefficients D_1 , D_2 , and D_3 in compartment regions 1,2, and 3, respectively. The goal is to evaluate the SD evolution at a point within region 1, as illustrated in Fig. 10, within a small time interval $[0, t_\varepsilon]$. It is assumed that the time interval is sufficiently small such that water molecules do not have time to travel beyond distance l , which l is the distance of point r' from the nearest boundary. By definition, the

propagator values will be equal to zero for all locations whose distances from r' are larger than l , which include regions 2 and 3. As a result, we have the following equalities,

$$\frac{\partial P_{r'}(r, t)}{\partial t} = D \nabla^2 P_{r'}(r, t) \xrightarrow{P_{r'}(r, t)=0} \quad (23)$$

$$0 = 0 D; \quad |r - r'| > l, \quad t \in [0, t_\varepsilon] \quad (24)$$

Eq. 24 is valid irrespective of all finite values of D , which implies that, during the small time interval, the original PDE is independent of the SD coefficient values in regions 2 and 3. In other words, D_2 and D_3 can be set to any arbitrary finite value, including D_1 . Hence, The environment can be considered with no layer boundaries.

REFERENCE

1. Stejskal, E.O., and J.E. Tanner. 1965. Spin diffusion measurements: spin echoes in the presence of time-dependent field gradient. *J Chem Phys.* 42:288-292.
2. Le Bihan, D., E. Berton, D. Lallemand, P. Grenier, E. Cbanis, and M. Laval-Jeantet M. 1986. MR imaging of intravoxel, incoherent motions: application to diffusion and perfusion in neurologic disorders. *Radiology.* 161: 401-407.
3. Mrboldt, K.D., W. Hnicke, and J. Frahm. 1985. Self-diffusion NMR imaging using stimulated echoes. *J. Magn. Reson.* 64:479-486.
4. Lee, J.S., M.K. Han, S.H. Kim, O.K. Kwon, and J.H. Kim. 2005. Fiber tracking by diffusion tensor imaging in corticospinal tract stroke: topographical correlation with clinical symptoms. *Neuroimage.* 26:771-776.
5. Yamada, K., H. Ito, H. Nakamura, O. Kizu, W. Akada, et al. 2004. Stroke patients' evolving symptoms assessed by tractography. *J Magn Reson Imaging.* 20:923-929.
6. Werring, D.J., A.T. Toosy, C.A. Clark, G. J. Parker, G. J. Barker et al. 2000. Diffusion tensor imaging can detect and quantify corticospinal tract degeneration after stroke. *J Neurol Neurosurg Psychiatry.* 69:269-272
7. Castriota-Scanderbeg, A., F. Fasano, G. Hagberg, U. Nocentini, M. Filippi, et al. 2003. Coefficient $D(av)$ is more sensitive than fractional anisotropy in monitoring progression of irreversible tissue damage in focal nonactive multiple sclerosis lesions. *AJNR Am J Neuroradiol.* 24:663-670
8. Bammer R., M. Augustin, S. Strasser-Fuchs, T. Seifert, P. Kapeller, et al. 2000. Magnetic resonance diffusion tensor imaging for characterizing diffuse and focal white matter abnormalities in multiple sclerosis. *Magn Reson Med.*44:583-591.
9. Yoshikawa K., Y. Nakata, K. Yamada, M. Nakagawa.2004. Early pathological changes in the parkinsonian brain demonstrated by diffusion tensor MRI. *J Neurol Neurosurg Psychiatry.* 75:481-484
10. Bozzali M., A. Falini, M. Franceschi, M. Cercignani, M. Zuffi, et al. 2002. White matter damage in Alzheimer's disease assessed in vivo using diffusion tensor magnetic resonance imaging. *J Neurol Neurosurg Psychiatry.* 72:742-746
11. Rose S.E., F. Chen, J. B. Chalk, F. O. Zelaya, W. E. Strugnell, et al. 2000. Loss of connectivity in Alzheimer's disease: an evaluation of white matter tract integrity with colour coded MR diffusion tensor imaging. *J Neurol Neurosurg Psychiatry.*69:528-530

12. Price, G. , M. S. Bagary, M. Cercignani, D. R. Altmann, M. A. Ron. 2005. The corpus callosum in first episode schizophrenia: a diffusion tensor imaging study. *J Neurol Neurosurg Psychiatry*.76:585–587.
13. Basser P.J., J. Mattiello, R. Turner, and D. Le Bihan.1994.Estimation of the effective self-diffusion tensor from the NMR spin echo. *J Magn Reson B*. 103:247:254.
14. Basser, P.J., J. Mattiello, R. Turner, D. Le Bihan.1994. MR diffusion tensor spectroscopy and imaging. *Biophys. J*. 66: 259-267
15. Sen, P.N., and P. J. Basser.2005. A model for diffusion in white matter in the brain. *Biophys. J*. 89:2927-2938
16. Berezhkovskii, A.M., G.H. Weiss. 2006. Diffusion in multilayer media: Transient behavior of the lateral diffusion coefficient. *J Chem Phys*. 124:154710
17. Stanotsz, G.J., A. Szafer, G.A. Wright, and R.M. Henkelman. 1997. An Analytical model of restricted diffusion in bovine optic nerve. *Magn Reson Med*.37:103-111
18. Sukstanskii, A.L., and D.A. Yablonska. 2002. Effect of restricted diffusion on MR signal formation. *J Magn Reson* 157:92-105
19. Szafer, A., J. Zhong, and J. C. Gore. 1995. Theoretical model for water diffusion in tissues. *Magn Reson Med*. 33:697-712
20. Ford, J.C., and D.B. Hackney.1997. Numerical model for calculation of apparent diffusion coefficients (ADC) in permeable cylinders- comparison with measured ADC in spinal cord white matter. *Magn. Reson. Med*. 37:387-394
21. Ford J.C., D.B. Hackney, E. Lavi, M. Phillips, and U. Patel. 1998. Dependence of apparent diffusion coefficients on axonal spacing, membrane permeability, and diffusion time in spinal cord white matter. *J. Magn. Reson. Imaging*. 8,:775-782.
22. Hwang, S.N., C.L. Chin, F.W. Wehrli, D.B. Hachney. 2003. An Image-based finite difference model for simulating restricted diffusion. *Magn. Reson. Med*. 50:373-382.
23. Solin P., K. Segeth, I. Dolezel. 2004.Higher-order finite element methods. Chapman & Hall/CRC
24. Callaghan, P.T. 1994. Principles of nuclear magnetic resonance microscopy. Oxford University Press
25. Haake E.M., R.W. Brown, M.R. Thompson, and R. Venkatesan. 1999. Magnetic Resonance Imaging: Physical Principles and Sequence Design. Wiley-Liss
26. Solin P. 2006. Partial differential equations and the finite element method. John Wiley & Sons, Inc. Hoboken, New Jersey.
27. Tuch, D.S. 2002. Diffusion MRI of complex tissue structure. Ph.D. dissertation, MIT.
28. Evans, L.E. 1998. Partial Differential Equations. American Mathematical Society

FIGURE LEGENDS

FIGURE 1

(left) A tetrahedral element used for discretization of this study, (right) a tetrahedralization of hexagonal array of cylinders model

FIGURE 2

(left) A cylinder model for a single axon, D_m and D_c represent constant SD coefficients for cytoplasm and myelin sheaths regions. (right) hexagonal organization of axons in WTs

FIGURE 3

Transverse SD propagation profile at the center of an axon cell (position 1 in Fig. 2). The bundle of axons orientation is considered along the z- axis, and the propagation is evaluated in the x-y plane after time elapses by 15 ms. The elevation of the graph represents the intensity of SD propagation

FIGURE 4

Parallel (along the z- axis) and transverse (along the y- axis) SD propagators as functions of spatial and temporal variables, for the axons organization in Fig. 2, (TOP) (left) time evolution of parallel propagator at position 1 in Fig. 2, (right) time evolution of transverse propagator at position 1 in Fig. 2, (BOTTOM) (left) Parallel propagators evaluated at different positions in Fig. 2 after 15 ms, (right) transverse propagators evaluated at different positions in Fig. 2, after 15 ms,

FIGURE 5

Validation of the propagator at center of an axon. The model coefficients for cytoplasm and myelin regions during computation of the FEM solution are set to $D_c = 0.6 \mu m^2/ms$, and $D_m = 0.015 \mu m^2/ms$, respectively, which are treated as ground truths. The curves are calculated by averaging the evaluations of Eq. 14 at different sample positions of each compartment, for each time instance. The standard deviations (sd) are provided to show the precision of the solution.

FIGURE 6

Voxel aggregate SD propagator for a single tract, after $t=15$ ms, (LEFT) (top) single WT passing through a voxel, (bottom) 1D parallel(along z- axis) and transverse(along y- axis) voxel aggregate propagator profiles, (MIDDLE) (top) 3D voxel aggregate propagator for the cytoplasm regions (bottom) 3D voxel aggregate propagator for the myelin regions, (RIGHT) (top) 3D voxel aggregate propagator for the extracellular regions, (bottom) 3D voxel aggregate propagator (average over all compartments). The values of 3D propagators are evaluated for displacement of $8 \mu m$ in all directions.

FIGURE 7

Voxel aggregate SD propagator with two crossing WTs

FIGURE 8

Effect of demyelination on SD propagator, (left) demyelinated axon, (middle) SD propagator at the position labeled by the red arrow, (right) SD propagator for the same position within a healthy axon

FIGURE 9

(top) a 2D element intersected by a layer boundary. The value of SD coefficient on the layer boundary has discontinuity which is discriminated by + and – subscripts. (bottom) organization of elements such that the layer boundary does not have any intersections which elements interior regions.

FIGURE 10

Three compartment SD environment

FIGURES

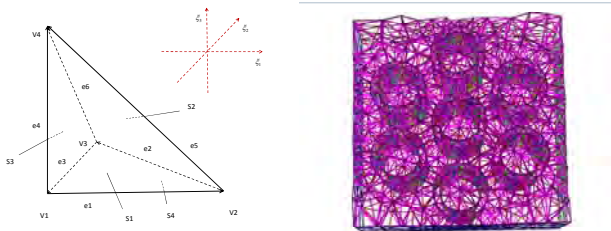


FIGURE 1

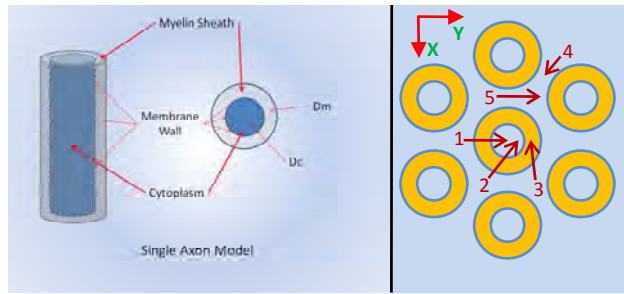


FIGURE 2

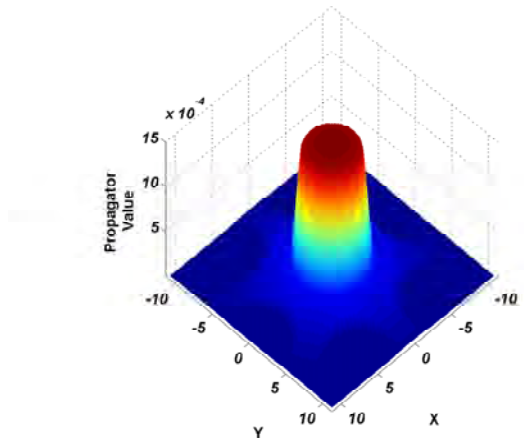


FIGURE 3

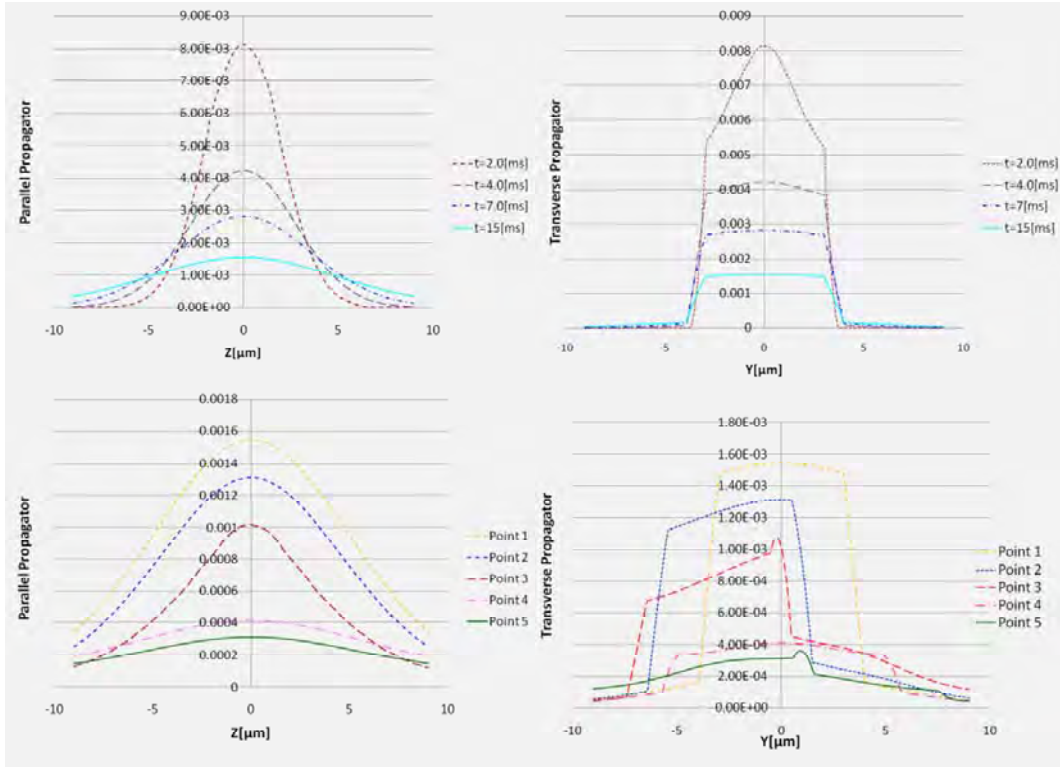


FIGURE 4

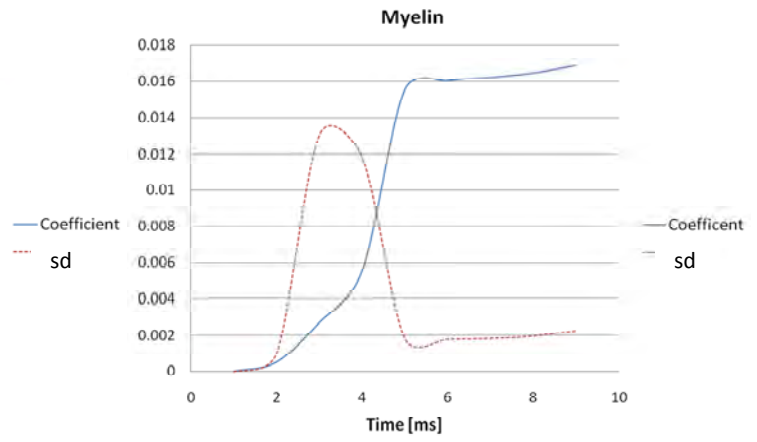
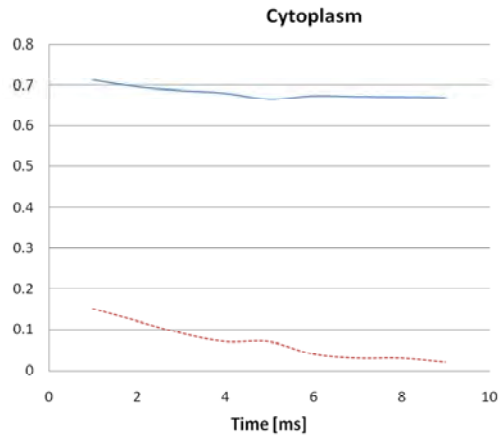


FIGURE 5

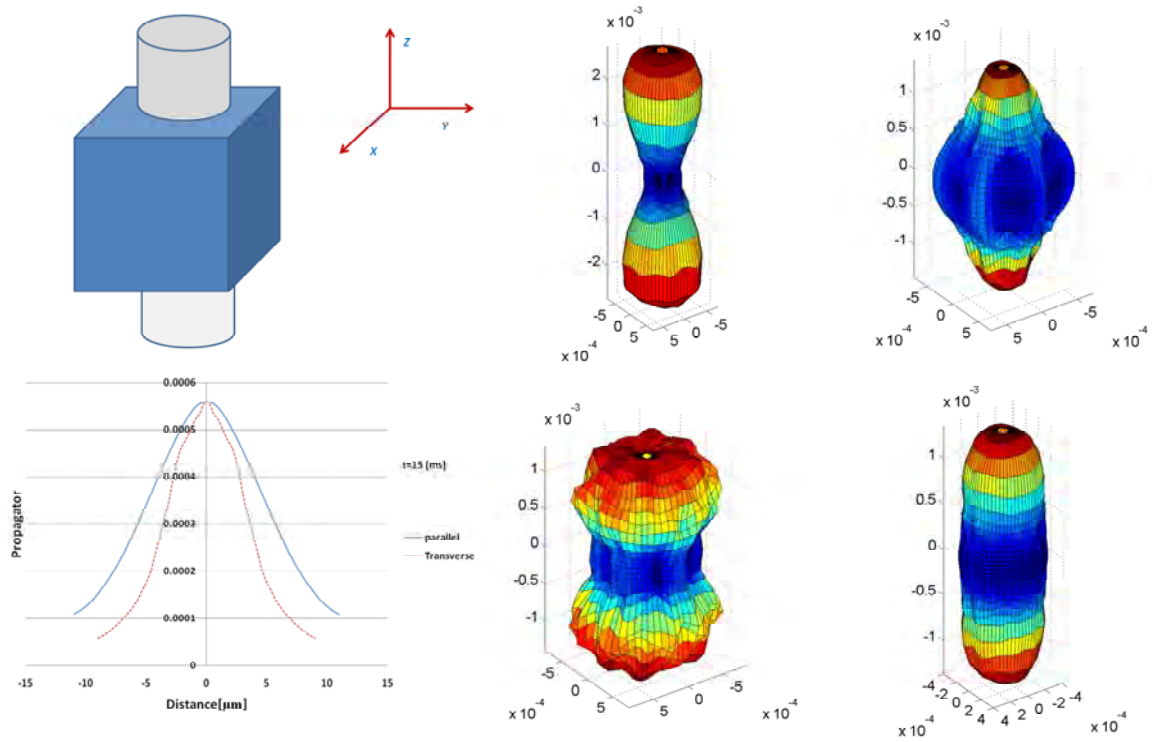


FIGURE 6

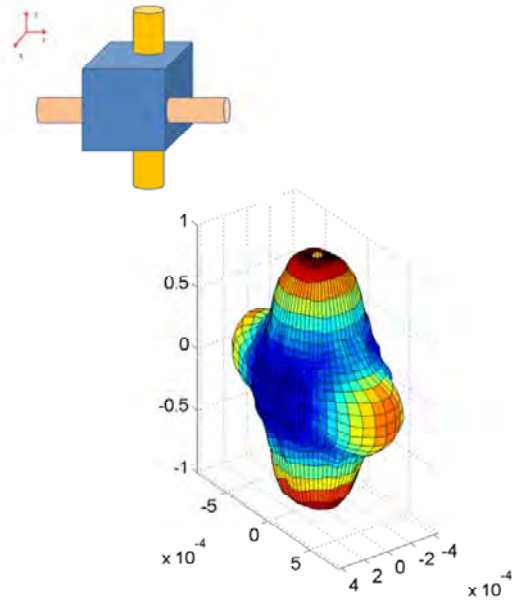


FIGURE 7

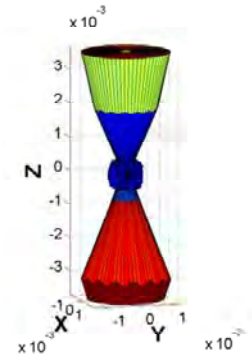
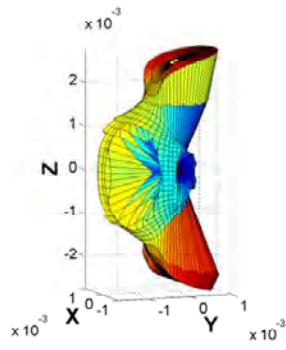
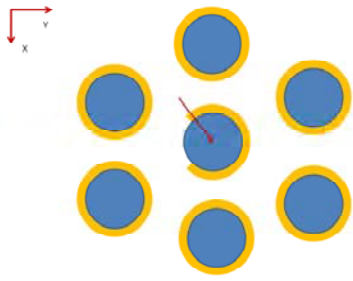


FIGURE 8

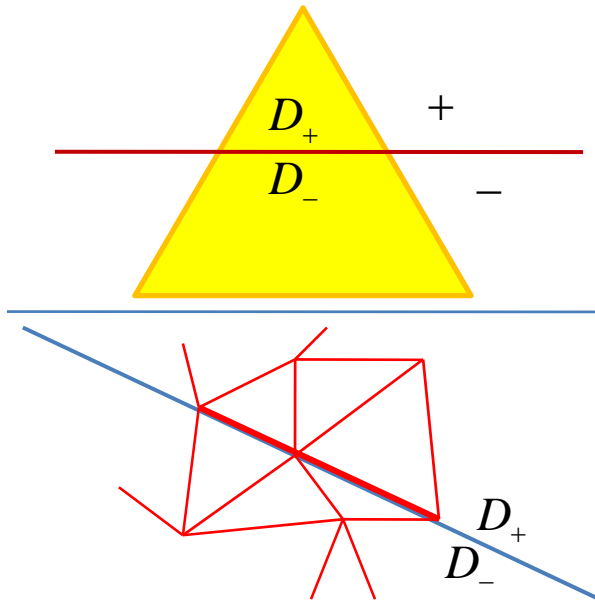


FIGURE 9

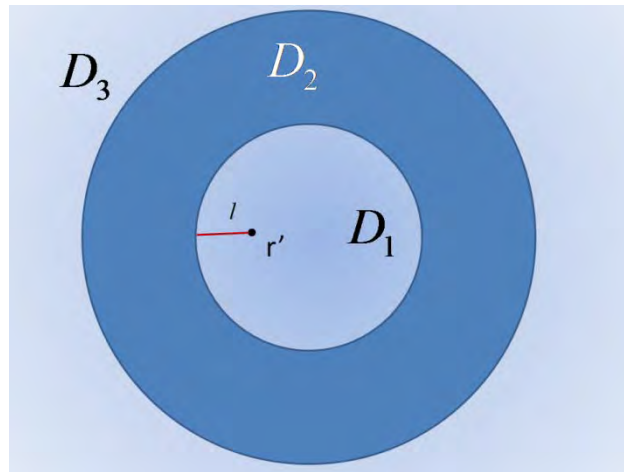


FIGURE 10